

1 Deep and rapid thermo-mechanical erosion by a  
2 small-volume lava flow

3 Gallant, E.<sup>1\*</sup>, Deng, F.<sup>1</sup>, Connor, C.<sup>1</sup>,  
Dixon, T.H.<sup>1</sup>, Xie, S.<sup>1</sup>, Saballos, J.A.<sup>2</sup>, Guitierrez, C.<sup>2</sup>,  
Myhre, D.<sup>3</sup>, Connor, L.<sup>1</sup>, Zayac, J.<sup>4</sup>, LaFemina, P.<sup>5</sup>, Charbonnier,  
S.<sup>1</sup>, Richardson, J.<sup>6,7</sup>, Maslervisi, R.<sup>1</sup>, and Thompson, G.<sup>1</sup>

- 1: University of South Florida, School of Geosciences  
2: Instituto Nicaragüense de Estudios Territoriales  
3: University of South Florida, College of Marine Science  
4: Queens College, Department of Earth and Environmental Sciences  
5: Pennsylvania State University, Department of Geosciences  
6: NASA Goddard Space Flight Center  
7: University of Maryland, Department of Astronomy

4 **Abstract**

5 We document remarkably efficient thermo-mechanical erosion by a small-  
6 volume lava flow. Downcutting by a basaltic-andesite lava flow on the  
7 steep-sided Momotombo volcano, Nicaragua, occurred at 100 times the  
8 rate commonly reported for thermal erosion in lava flow fields, even though  
9 this flow was small-volume (0.02 km<sup>3</sup>) and effused at a low rate for <1  
10 week. The erosion depth, up to 30 m incision, is explained by reduction of  
11 hardness,  $H$ , of the pyroclastic substrate into which the lava flow incised.  
12 We show that incision depth decreases, approximately exponentially, with  
13 distance along the flow path, until erosion stopped and the flow became  
14 constructional. This transition occurs 650 m from the vent on a slope  
15 averaging a 32° incline. Results indicate that syn-eruptive erosion is an  
16 important morphological process on some steep-sided volcanoes that are  
17 predominantly composed of layered pyroclasts. Rapid erosion and incision  
18 increased flow run-out for the 1905 flow, which in turn directed the flow  
19 and run-out of the 2015 lava flow. Mapping and understanding these fea-  
20 tures is critical for improving lava flow hazard assessments and provides  
21 insight into the construction and growth of composite cones.

22  
23 **Keywords:** lava flow physics; thermal and mechanical erosion; lava in-  
24 undation; volcano morphology; remote sensing; thermal dynamics of lava

25  
26 Corresponding Author: [egallant@usf.edu](mailto:egallant@usf.edu)

27 *Non-peer reviewed preprint submitted to EarthArXiv and Elsevier*

## 28 **1 Introduction**

29 Lava flows are responsible for altering landscapes on geologically short timescales.  
30 The overwhelming majority of lava flows construct topography by building  
31 raised channels and/or compound flow fields, both of which evolve through  
32 time and along-flow (Kerr et al., 2006; Dietterich and Cashman, 2014). The  
33 morphologies of flow features are mainly determined by the composition and ef-  
34 fusion rate of the flow, as well as the pre-existing and syn-eruptive topography  
35 (Richardson and Karlstrom, 2019; Bilotta et al., 2019). These factors also con-  
36 trol the thickness of lava flows, which in turn influence a flow’s run-out distance  
37 and inundation hazard potential (Kilburn and Lopes, 1988; Dietterich et al.,  
38 2017). A small fraction of channelized flows and lava tubes erode into older  
39 surfaces during emplacement via thermal, mechanical, or thermo-mechanical  
40 processes (Greeley et al., 1998; Fagents and Greeley, 2001; Kerr, 2001; Siewert  
41 and Ferlito, 2008; Hurwitz et al., 2010, 2013).

42 The 1905 eruption of Momotombo volcano, Nicaragua, provides an exam-  
43 ple of thermo-mechanical erosion by a small volume ( $<0.02 \text{ km}^3$ ) lava flow on  
44 a steep-sided edifice (Figs. 1 and 2). We first document the morphology of  
45 the channel using a combination of satellite and terrestrial radar generated dig-  
46 ital elevation models (DEMs) from 2012–2017. Erosion depths from the 1905  
47 flow are then calculated by reconstructing pre-channel topography, extracting  
48 cross-sectional profiles, and calculating the maximum difference between the  
49 measured and modeled surfaces normal to the channel. We use these results  
50 to test thermal and thermo-mechanical models of erosion. Model inputs are in-  
51 formed by observations from Momotombo’s most recent eruption in 2015, which  
52 we capture with the range of our satellite observations. We find the channel was  
53 thermo-mechanically eroded by a lava flow that erupted in 1905. Additionally,  
54 we assert that thermo-mechanical erosion is an important morphological process

55 on some steep-sided volcanoes composed predominantly of layered pyroclasts.  
56 This study is the first to look at lava flow erosion on steep sided slopes, expands  
57 our knowledge of the rate at which syn-eruptive erosion occurs, and mathemat-  
58 ically couples thermal and mechanical models of erosion.

## 59 **2 Background**

### 60 **2.1 Erosion by Lavas**

61 Erosion by lava has been hypothesized for the formation of rilles on both Mars  
62 (Dundas and Keszthelyi, 2014) and the Moon (Head and Wilson, 2017; Wilson  
63 and Head, 2017), canali on Venus (Baker et al., 1992; Williams-Jones et al.,  
64 1998), and channels on Io (Schenk and Williams, 2004). Studies of active erosion  
65 by flowing lava have occurred on the island of Hawai‘i during the 1972–1974  
66 Mauna Ulu eruption and the initial stages of the 1983-2018 Pu‘u O‘o eruption,  
67 where erosion rates of 4 cm depth/day and 10 cm depth/day were observed in  
68 lava tubes via skylights, respectively (Peterson et al., 1994; Kauahikaua et al.,  
69 1998). Erosion by turbulent komattite flows during the Archean, responsible  
70 for large Ni-sulphide ore deposits, is also widely noted (Williams et al., 1998;  
71 Beresford et al., 2002; Staude et al., 2017).

### 72 **Thermal Erosion**

73 Thermal erosion occurs when lava moves with sufficient flux and temperature to  
74 melt and incise the underlying terrain (Kerr, 2001). Thermal erosion by flowing  
75 lava requires the complete or partial melting and assimilation of a substrate  
76 into the overriding flow. A lava flow’s total available thermal energy ( $E_{thermal}$ ),  
77 sourced from advection and crystallization, is modeled as:

$$E_{thermal} = m_l[c_{pl}(T_l - T_a) + \phi F] \quad (1)$$

78 where  $m_l$  is the mass of the erupted lava,  $c_{pl}$  is the specific heat capacity of  
 79 the lava,  $T_l$  is the erupted temperature of the lava,  $T_a$  is the temperature of the  
 80 environment into which heat is being transferred (the substrate in this case),  $\phi$   
 81 is the mass fraction crystallization, and  $F$  is the latent heat of fusion (Wooster  
 82 et al., 1997). Lava flows are an open system where available thermal energy  
 83 is eventually balanced out by heat loss through conduction, convection, and  
 84 radiative heat transfer. Studies of the thermal energy balance of lava flows on  
 85 Mt Etna show that upwards of 85% of energy was retained during the initial  
 86 phases of the eruption, which can be used to further bound the amount of energy  
 87 available to melt and erode the substrate (Wooster et al., 1997; Patrick et al.,  
 88 2004). The presence of multiple heat sinks also highlights the fact that not all  
 89 available thermal energy can be partitioned into eroding the substrate, so we  
 90 need to quantify heat transfer between the base of the lava flow and substrate.  
 91 The rate of conductive heat transfer into the substrate (i.e., the growth of a  
 92 thermal boundary layer) can be modeled as:

$$\frac{dy}{dt} = \frac{\eta_T \sqrt{\kappa}}{t} \quad (2)$$

93 where  $y$  is the depth into the substrate,  $t$  is the duration of the flow, and  $\eta_T$  is  
 94 a dimensionless similarity variable (Turcotte et al., 2002; Fagents and Greeley,  
 95 2001). The growth of this boundary layer is illustrated in Figure 3.

## 96 **Mechanical Erosion**

97 Mechanical erosion occurs when the wearing material (the lava flow) is harder  
 98 than the substrate (the edifice) (Sklar and Dietrich, 1998; Siewert and Ferlito,  
 99 2008; Hurwitz et al., 2010). The early stages of an eruption are most conducive



100 to erosion because flow velocity is often highest and basal friction is also high due  
 101 to the vertical load (Siewert and Ferlito, 2008; Hurwitz et al., 2010). Mechanical  
 102 erosion as a function of substrate hardness can be modeled as:

$$H = \frac{k\rho ghvtsin\theta}{d_{channel}} \quad (3)$$

103 where  $H$  is the hardness of the substrate,  $k$  is a dimensionless proportionality  
 104 constant that captures the material hardness of the erosive layer (the lava flow),  
 105  $\rho$  is the density of the lava flow,  $h$  is the thickness of the lava flow,  $v$  is the  
 106 velocity of the lava flow,  $\theta$  is the slope of the edifice, and  $d_{channel}$  is the depth  
 107 of erosion. This equation implies that the depth of an eroded channel will be  
 108 constant, so long as the velocity of the flow is constant. If the depth of the  
 109 channel changes with distance, then either the velocity of the flow is changing,  
 110 or the hardness,  $H$ , is changing, or both.

111 The yield strength is an exponential function of temperature, which means  
 112 that  $H$  can also be modeled as a function of temperature:

$$H \approx \frac{ae^{(-bT_a)}}{3} \quad (4)$$

113 where  $a$  and  $b$  are flow-dependent variables that vary with magma composition  
 114 and  $e$  is Euler's number. This relationship describes softening of the substrate  
 115 as temperature increases or for a longer duration of heating, which means that  
 116 mechanical lava erosion models presented in Siewert and Ferlito (2008) can be  
 117 reworked to become thermo-mechanical models. Values of  $1.18 \times 10^5$  Pa and  
 118  $0.12 \text{ K}^{-1}$  correspond to  $a$  and  $b$  for Momotombo. We note that experimental  
 119 data have indicated that the Arrhenius relationships shown in Equation 4 break  
 120 down around the glass transition point (Miller, 1963; Gottsmann and Dingwell,  
 121 2002).

## 122 **2.2 Geology of Momotombo and Recent Activity**

123 Momotombo (1,297 m) is located at the southern end of the Cordillera de Los  
124 Maribios in central Nicaragua (Fig. 1). The edifice is composed primarily of  
125 basaltic to basaltic andesite lavas, cinders, and other tephra that erupted dur-  
126 ing the last 4,500 years (Kirainov et al., 1988). Sixteen historical eruptions  
127 have been documented, the majority of which have been strombolian to violent  
128 strombolian (VEI 1-2), with several plinian events (up to VEI 4) (Global Vol-  
129 canism Program, 2017). A VEI 4 eruption in 1605-1606 and large earthquake in  
130 1610 lead to the abandonment of city of León (Viejo), the capitol of the region  
131 at that time (Sapper, 1925). Though the specific morphological changes to the  
132 edifice from the 1605-1606 plinian event are not well documented, it's possible  
133 that serious damage to the structural integrity of the summit occurred given the  
134 impact on surrounding municipalities (Sapper, 1925). The subsequent steady  
135 activity throughout the 1800's rebuilt the summit from cinders, agglutinate,  
136 and channelized lava flows, as shown in photographs from the late 1800's and  
137 early 1900's (Vincent, 1890; Intercontinental Railway Commission, 1898; Sap-  
138 per, 1925). Analogous volcanoes, such as Ngauruhoe (New Zealand) (Hobden  
139 et al., 2002), Izalco (El Salvador) (Carr and Pontier, 1981), and Cerro Negro  
140 (Nicaragua) (Hill et al., 1998; Courtland et al., 2012), have built moderately  
141 sized pyroclastic cones in only a few hundred years and can provide insight into  
142 the constructional history of Momotombo.

143 The 1905 eruption (VEI 2) occurred between January 16–21 (Sapper, 1925).  
144 The basaltic andesite lava flow was accompanied by an eruptive column of suf-  
145 ficient height to deposit ash 15 km to the west on the city of León. The effusive  
146 component consisted of an eruptive volume of  $<0.02 \text{ km}^3$  of basaltic andesite  
147 (Fig. 1). Intermittent explosions occurred that sent incandescent blocks and  
148 bombs "a great distance" from the crater (Sapper, 1925). First person accounts

149 also describe destruction to the summit during the eruption, which may have  
150 resulted in the drainage of a small summit lava lake (Sapper, 1925) (Fig. 2).  
151 The 1905 eruption was followed by 110 years of quiescence, which ended on 30  
152 November, 2015. A small volume basaltic andesite lava flow was emplaced be-  
153 tween 1 December and 7 December, 2015, and was followed by several months  
154 of intermittent explosions (Global Volcanism Program, 2017).

## 155 **3 Methods and Results**

### 156 **3.1 Digital Elevation Model Generation**

#### 157 **3.1.1 TanDEM-X Satellites**

158 Digital elevation models (DEMs) were generated from TanDEM-X Satellites  
159 (TDX) and collected on 24 October, 2012 and 18 March, 2017. These DEMs,  
160 which also capture the change in topography due to the eruption in 2015–2016,  
161 allow us to obtain baseline measurements for the 1905 channel (Fig. 4) and  
162 determine if any erosion occurred during the most recent eruption. The bistatic  
163 mode of TDX allows these two satellites to fly in tandem formation and observe  
164 the same ground point simultaneously (Krieger et al., 2007). We note that the  
165 flight paths for these acquisitions were not the same, which resulted in an offset  
166 due to a heading difference of  $\sim 21^\circ$ .

167 GAMMA software was used to process the TDX SAR images to generate  
168 DEMs with the InSAR (Interferometric Synthetic Aperture Radar) technique  
169 (e.g., Deng et al., 2019). A 30-m SRTM (Shuttle Radar Topography Mission)  
170 DEM provided independent ground control points. Two (range) by two (az-  
171 imuth) pixel multilooking was used to reduce speckle noise. The final DEMs  
172 have a spatial resolution of  $5 \times 5$  meters with a vertical precision of  $< 2$  m.

### 173 **3.1.2 Terrestrial Radar**

174 We employed terrestrial radar interferometry (TRI) to assess the level of noise  
175 in our topographic profiles (described below) from the 2017 TDX acquisition.  
176 Although this comparison does not give us a direct assessment of noise for the  
177 2012 DEM (the model from which we are measuring channel incision depths),  
178 it gives a relative level of confidence in our TDX DEM processing methods.  
179 TRI is a ground-based scanning radar that measures the amplitude and phase  
180 of a backscattered microwave signal. A GAMMA real aperture radar operating  
181 at Ku-band (1.74 cm wavelength) was used for this study. The TRI has one  
182 transmitting antenna and two receiving antennas, which allows for topographic  
183 mapping with a single scan (e.g. Dixon et al., 2012; Caduff et al., 2015; Voytenko  
184 et al., 2015; Xie et al., 2018; Deng et al., 2019). The resolution of the range  
185 measurements is  $\sim 1$  m, and the azimuth resolution varies linearly with distance  
186 (e.g., 1.8 m at 1 km distance, 7 m at 4 km). The spatial coverage of TRI is much  
187 smaller compared to satellite imaging. Details of TRI data processing for DEM  
188 generation are given in Strozzi et al. (2012) and Xie et al. (2018). TRI surveys  
189 were conducted in December 2015 and April 2016. We use results from the  
190 2016 campaign because it occurred towards the end of the eruption period and  
191 is temporally closer to the 2017 TDX acquisition. The TRI DEM has a  $5 \times 5$  m  
192 resolution with an accuracy  $< 5$  m and covers the incised portion of the channel  
193 (Fig. 5).

### 194 **3.2 Channel Profiles and Depth Calculation**

195 Previous GIS-based methods used to determine paleotopography of volcanic  
196 terrains (e.g., Germa et al., 2015) interpolate missing topography based on  
197 connecting high points in elevation. Studies of fluvial channel erosion in steep  
198 terrain generally do not deal with incision into conical edifices (Robl et al., 2008;

199 Fox, 2019). Additionally, these approaches model down-section and not cross-  
200 section morphology, which we require to accurately measure incision depth and  
201 extract cross-section profiles. We developed an elliptical least-square best-fit  
202 contour method to obtain incision depths along the channel on Momotombo's  
203 steep slopes to fill this application gap. We use this method to obtain channel  
204 depths and cross-channel profiles from the 2012 and 2017 TDX DEMs and the  
205 2016 TRI DEM. Our depth measurements are minimum values, as it is likely  
206 that the eroding flow would have emplaced some volume of lava within the  
207 channel. We also use this method to determine if any incision occurred during  
208 the 2015 lava flow. Additionally, comparing the post-2015 TDX and TRI DEMs  
209 provides an indication of noise within our channel measurements.

210 This approach measures incision depth against modeled paleotopography  
211 created from optimized elliptical contours. A path down the channel's center  
212 was defined with a sampling density set to the resolution of the DEM (5 m  
213 for this study)(Fig. S1a). The widths of the channel and levees, determined  
214 visually, were masked out in order to separate their signal from the overall signal  
215 of the cone. A refined elliptical fit for the uppermost contour of the channel path  
216 was calculated by minimizing the mean-squared difference between the actual  
217 elevation contour and an elliptical contour. This optimized ellipse was then used  
218 to calculate a fit to the elevation contour below. This second recalculated ellipse  
219 was then fit to the next elevation contour, and so forth, until the end of the  
220 designated channel path was reached. The output of this process is a modeled  
221 paleotopography with no channel or levee structures (Fig. S1b). The incision  
222 depth was calculated against the modeled paleotopography. The normal vector  
223 to the paleotopographic model was calculated at each point, spaced 5 m apart  
224 along each elliptical contour. As before, the normal vector was calculated by  
225 fitting a plane to 8 adjacent points (three from the contour above, three from

226 the contour below, and two adjacent points from the same contour) (Fig. S1c).  
227 The DEM was then re-orientated such that the z-axis was coincident with the  
228 calculated normal vector. The incision depth was returned as a weighted average  
229 of the constituent points, with weighting criteria based on the distance of the  
230 points to the center of the plane (i.e., the point closest to the center had the  
231 greatest weight) (Fig. S1d). This process was repeated for each point along the  
232 contour, and then for every contour. This process allowed us to measure the  
233 incision depth throughout the channel while removing the conic signal of the  
234 edifice (Fig. 6). Incision depth varied from 35 m at the summit rim and tapers  
235 off to 0 at  $\sim 600$  m elevation (Fig. 7). We calculate the eroded volume of the  
236 channel to be  $4 \times 10^5$  m<sup>3</sup>. A profile of each cross-channel contour was calculated  
237 for the 2012 and 2017 TDX and 2016 TRI DEMs (Fig. 8).

238 Results show the pre-2015 eruption channel extended down the northeast  
239 side of the edifice from the summit and incised into the summit (Fig. 6). The  
240 2015 lava flow follows the same path as the pre-eruption channel (Fig 8). The  
241 elliptical contour fit method was also applied to the 2016 TRI DEM. Data gaps  
242 within the DEM were filled using a regularized spline with tension interpolation  
243 method in QGIS and the same process described above was utilized. We provide  
244 the code for this method (S1) and an additional code for a circular fit method  
245 in the Supplemental Documentation (S2).

## 246 4 Discussion

### 247 4.1 Channel Origins

248 The difference between modeled paleotopography and the 2012 TDX DEM  
249 shows that a channel has cut into the edifice. The distribution of lava flows  
250 beneath the 1905 units, shown in Figure 1, implies that no structure existed in

251 this location prior to 1905 to consistently direct the path of subsequent lava flows  
252 (as was the case for the 2015 eruption). No historical reports note a leveed lava  
253 channel on the NE flank of Momotombo prior to the 1905 eruption (Vincent,  
254 1890; Intercontinental Railway Commission, 1898; Sapper, 1925). Examination  
255 of the area surrounding Momotombo shows no down-slope deposition of suffi-  
256 cient volume to support a channel having carved into the NE edifice prior to the  
257 1905 eruption by environmental erosion (e.g. hydrologic erosion) and then in-  
258 filled by subsequent lava flows. The rest of the edifice is similarly devoid of any  
259 large-scale drainage features (e.g. barrancas, rilles, or gullies). DEM analyses  
260 show the channel width is uniform from summit to low on the slopes (Fig. 2a).  
261 Incised channels on other volcanoes (e.g., Merapi, Nevado del Ruiz) are gener-  
262 ally much wider at the mouth, less consistent in width, and are less linear than  
263 Momotombo's channel because they are related to more violent hazards (e.g.,  
264 pyroclastic density currents and lahars). Results also show it was unlikely that  
265 erosion occurred during the 2015 lava flow, given that it flowed over the armored  
266 channel and not a variably consolidated slope of cinders and spatter/agglutinate  
267 (Fig. 7). In the absence of evidence that suggests otherwise, we conclude that  
268 channel most likely formed during the emplacement of the 1905 lava flow.

#### 269 **4.1.1 Thermal Erosion**

270 The total energy emitted by the 1905 lava flow, calculated using Equation 1,  
271 is about  $7 \times 10^{16}$  J for an eruptive volume of  $2 \times 10^7$  m<sup>3</sup>. Taking into account  
272 the energy balance between heat sources (85% retained) and sinks (15% lost)  
273 described in Wooster et al. (1997), we calculate that  $6 \times 10^{16}$  J is the minimum  
274 amount of the original energy that remained within the flow. Although the  
275 length of time used to calculate this ratio for the Mount Etna eruption was  
276 greater than the duration of the Momotombo eruption, it is helpful to place a  
277 first order constraint on how much thermal energy is lost into the environment.

278 We calculate the total energy needed to fully erode the channel is about 2  
279  $\times 10^{14}$  J, by substituting the mass of the eroded section of the channel into  
280 Equation 1. Although we find that sufficient energy exists within the system  
281 to erode the substrate, we note that not all of the energy present is available  
282 for this purpose. Had all of this energy been used to erode, the thermal loss  
283 would have been sufficiently great that the emplaced flow would be much thicker  
284 and shorter than what is observed. Modeling the depth of heat transfer into  
285 the substrate as a function of time using Equation 2 estimates the growth of  
286 the substrate thermal boundary layer at 8.8 cm per day. Thermal erosion rates  
287 in Hawaiian tubes and channels can reach  $\sim 10$  cm per day (Kauahikaua et al.,  
288 1998); given the lower temperature of lavas erupted on Momotombo, a slower  
289 rate of thermal boundary layer growth makes sense. Given the short duration of  
290 the 1905 eruption ( $< 1$  week; Sapper, 1925), thermal erosion by itself is unlikely  
291 to have formed the observed morphology.

#### 292 **4.1.2 Thermo-mechanical Erosion**

293 Conceptually, once the near-subsurface reaches the threshold temperature, which  
294 we assert is the glass transition (1013 K, Giordano et al., 2005), the hotter sub-  
295 surface material is transported downhill by the lava flow. For this assumption  
296 to be correct, the slope has to be steep and the lava flow velocity at its base has  
297 to be fast. This implies that the thermal boundary layer reaches some critical  
298 thickness and is then eroded away mechanically by the lava flow. While this  
299 process surely contributes to incision of the channel, it cannot fully account for  
300 the observed depths. It is possible  $H$  varies with distance along the channel  
301 because the underlying substrate changes from very soft material at the top of  
302 the cone to harder material lower on the flanks. We reject this because the sur-  
303 face of the edifice is a relatively uniform slope without major lithologic changes.  
304 These results provide insight into how heat is transferred into the substrate over



305 time, which helps us understand how the material hardness of the substrate,  $H$ ,  
306 is reduced over time as the lava flow moves downslope.

307 We assume that the growth and removal of the thermal boundary layer over  
308 time can be approximated as a steady state process, captured by the depth  
309 of incision at each point along the channel. An exponential was fit to the  
310 incision depth data to extract the quadratic function of  $d_{channel}$  in terms of  
311 incision depth and elevation (Fig. 10). We solve for  $H$  and find that the lowest  
312 value (corresponding to softest substrate) was  $4.8 \times 10^5$  Pa corresponding to  
313 an incision depth of 30 m (Fig. 10). These results show the hardness of the  
314 substrate increases as a function of time, but note that we use depth as proxy  
315 for time. Realistically, the deepest incision points are closest to the vent because  
316 they have been exposed to erosive work for a greater amount of time. The  
317 function modeled to from Equation 3 tackles that problem from the opposite  
318 perspective (i.e., it models the decrease in erosive depth, which suggests increase  
319 in hardness). We know that temperature is increasing in the substrate based on  
320 the relationships described in Equation 2, which decreases the hardness, so we  
321 revise these results and report them as a decrease in hardness over time to more  
322 accurately reflect the physical processes controlling the incision depth. Detailed  
323 historical observations list the eruption duration as six to seven days in length,  
324 which allows us to place constraints on the rate of change of hardness (Fig. 9)  
325 (Sapper, 1925).

## 326 4.2 Channel Growth

327 We calculate that the eroded volume is equal to roughly 2% of the total volume  
328 of the 1905 lava flow. Given the low eruptive temperature of basaltic andesites, it  
329 is unlikely that this material was fully assimilated into the flow. As the material  
330 heats and softens it is likely dragged downslope along the base of the flow for

331 a short distance and then re-deposits, which creates a scalloped type signal for  
332 the measure of incision depth against elevation (Fig. 7). The thicknesses of  
333 subsequent lava flows will respond to this subtle topographic variability (i.e.,  
334 more lava will be deposited in the troughs, less on the crest), which we find to  
335 be true for the 2015 flow (Fig. 7). We also note a strong correlation between  
336 incision and lack of developed levees in the 2012 TDX DEM, which suggests that  
337 erosion began early on during the eruption (Fig. 8, conceptualized in Fig. 12).  
338 This implies that levee bounded incised channels are not thermo-mechanically  
339 eroded, which is an important consideration for studies of incised channels on  
340 other planetary bodies.

### 341 **4.3 Morphologic Implications**

342 The depth of a thermally eroded channel is limited by the efficiency of heat  
343 transfer across the boundary between the lava flow and the substrate, the rate  
344 of heat transfer in the subsurface, and the duration of an eruption (Kerr, 2001);  
345 when combined with morphologic studies of emplacement conditions (especially  
346 time), a constraint can be placed on the maximum depth of erosion. Channels  
347 whose incision depth exceeds this threshold indicate a preferential hardness  
348 ratio of the substrate to the flow (i.e., it is softer than the overriding flow) and  
349 can therefore be used to determine the presence of pyroclastic rocks and other  
350 easily eroded terrain (e.g., unconsolidated regolith, alluvial deposits, etc.) on  
351 planetary surfaces that can only be observed remotely. Large flows on the Moon,  
352 in particular, may be worth revisiting in light of these findings (Hurwitz et al.,  
353 2013).

354 A 1528 drawing of Momotombo by Oviedo (Fernandez de Oviedo y Valdes,  
355 1528) shows a similar channel on the volcano's west side. A channel on the  
356 northern flank (likely emplaced during an eruption in the second half of the

357 1800's Sapper (1925)) is also incised into the cone, and has been infilled by cin-  
358 ders from subsequent eruptions, which suggests the processes of slope incision  
359 and subsequent infill occurs with relative frequency on Momotombo. The pref-  
360 erential diversion of lava flows into incised channels for future events suggest  
361 that lava flow hazards on some steep-sided volcanoes are influenced by the cre-  
362 ation, infill, and eventual abandonment of these structures. The channel may  
363 limit the lava flow hazard for the western flank if the next eruption is similar in  
364 size. Understanding the evolution of these features has important implications  
365 for lava flow hazards and growth patterns and erosion of composite volcanoes.

## 366 5 Conclusions

367 We use satellite (TDX) and terrestrial radar (TRI) DEMs to obtain a detailed  
368 record of recent changes to the edifice of Momotombo Volcano from 2012–2017,  
369 during which a VEI-2 eruption occurred. We describe a unique lava channel  
370 that incised 25–35 m into the northeast sector of the volcano near the summit  
371 and transitions into a constructional channel roughly halfway down the edifice.  
372 We assert that this feature formed erosively during the emplacement of a lava  
373 flow in 1905 and note a direct correlation between a lack of levees and incision  
374 depth. Thermal erosion alone was unable to account for the full depth of incision  
375 and we suggest that thermo-mechanical erosion is the likely cause. We examine  
376 inputs from mechanical models of erosion and determine that, based on the  
377 relationship between material hardness and shear strength, these models should  
378 be re-classified as thermo-mechanical. We propose that the transfer of heat into  
379 the substrate decreases the hardness of the material, which encourages it to  
380 flow more readily and excavate. We establish that the critical temperature at  
381 which this occurs is lower than previously thought, likely at the glass transition  
382 temperature (1013K), instead of the liquidus of a given lava. We calculate the

383 total eroded volume to be  $4 \times 10^5 \text{ m}^3$  and determine a minimum hardness of 4.8  
384  $\times 10^5 \text{ Pa}$  at the deepest point of incision for the 1905 eruption. Deeply incised  
385 channels control the distribution of future flows and can also be used to infer  
386 the material properties of the substrate into which they are excavated.

## 387 **Acknowledgments**

388 Funding for field work was provided by NSF EAR 1620977: Geochemical and  
389 Geophysical Observations of the 2015 Eruption of Volcan Momotombo, Nicaragua,  
390 awarded to PL, CC, and others. Field support was provided by many staff at  
391 INETER. Equipment logistics were eased by the efforts of Denis Voytenko and  
392 Milton Ordonez. The manuscript's clarity was improved by feedback from Jen  
393 Bright, facilitated by Pam Wayne and Jose Rincon.

## 394 References

- 395 Baker, V. R., Komatsu, G., Parker, T. J., Gulick, V. C., Kargel, J. S., and  
396 Lewis, J. S. (1992). Channels and valleys on Venus: Preliminary analysis of  
397 Magellan data. *Journal of Geophysical Research. Planets*, 97(E8):13421.
- 398 Beresford, S., Cas, R., Lahaye, Y., and Jane, M. (2002). Facies architecture of an  
399 archean komatiite-hosted ni-sulphide ore deposit, victor, kambalda, western  
400 australia: implications for komatiite lava emplacement. *Journal of Volcanol-  
401 ogy and Geothermal Research*, 118(1):57 – 75.
- 402 Bilotta, G., Cappello, A. and Herault, A., and Del Negro, C. (2019). Influ-  
403 ence of topographic data uncertainties and model resolution on the numerical  
404 simulation of lava flows. *Environmental Modelling and Software*, 112:1–15.
- 405 Caduff, R., Schlunegger, F., Kos, A., and Wiesmann, A. (2015). A review of ter-  
406 restrial radar interferometry for measuring surface change in the geosciences.  
407 *Earth Surface Processes and Landforms*, (2):208.
- 408 Carr, M. J. and Pontier, N. K. (1981). Research paper: Evolution of a young  
409 parasitic cone towards a mature central vent; Izalco and Santa Ana volcanoes  
410 in El Salvador, Central America. *Journal of Volcanology and Geothermal  
411 Research*, 11:277 – 292.
- 412 Courtland, L. M., Kruse, S. E., Connor, C. B., Connor, L. J., Savov, I. P.,  
413 and Martin, K. T. (2012). Gpr investigation of tephra fallout, cerro negro  
414 volcano, nicaragua: a method for constraining parameters used in tephra  
415 sedimentation models. *Bulletin of Volcanology*, (6):1409.

- 416 Deng, F., Rodgers, M., Xie, S., Dixon, T. H., Charbonnier, S., Gallant, E. A.,  
417 Vlez, C. M. L., Ordoez, M., Malservisi, R., Voss, N. K., and Richardson,  
418 J. A. (2019). High-resolution dem generation from spaceborne and terrestrial  
419 remote sensing data for improved volcano hazard assessment a case study at  
420 nevado del ruiz, colombia. *Remote Sensing of Environment*, 233:111348.
- 421 Dietterich, H., Lev, E., Chen, J., Richardson, J., and Cashman, K. (2017).  
422 Benchmarking computational fluid dynamics models of lava flow simulation  
423 for hazard assessment, forecasting, and risk management. *Journal of Applied*  
424 *Volcanology*, 6(1):1.
- 425 Dietterich, H. R. and Cashman, K. V. (2014). Channel networks within lava  
426 flows: Formation, evolution, and implications for flow behavior. *Journal of*  
427 *Geophysical Research. Earth Surface*, 119(8):1704.
- 428 Dixon, T. H., Voytenko, D., Lembke, C., Pea, S., Howat, I., Gourmelen, N.,  
429 Werner, C., and Oddsson, B. (2012). Emerging technology monitors ice-sea  
430 interface at outlet glaciers. *Eos (0096-3941)*, 93(48):497.
- 431 Dundas, C. M. and Keszthelyi, L. P. (2014). Emplacement and erosive effects  
432 of lava in south Kasei Valles, Mars. *Journal of Volcanology and Geothermal*  
433 *Research*, 282:92 – 102.
- 434 Fagents, S. A. and Greeley, R. (2001). Factors influencing lava-substrate heat  
435 transfer and implications for thermomechanical erosion. *Bulletin of Volcanol-*  
436 *ogy*, (8):519.
- 437 Fernandez de Oviedo y Valdes, G. (1528). Infierno de mamea.
- 438 Fox, M. (2019). A linear inverse method to reconstruct paleo-topography. *Ge-*  
439 *omorphology*, 337:151 – 164.

- 440 Germa, A., Lahitte, P., and Quidelleur, X. (2015). Construction and destruc-  
441 tion of Mont Pele volcano: Volumes and rates constrained from a geomorpho-  
442 logical model of evolution. *Journal of Geophysical Research. Earth Surface*,  
443 120(7):1206.
- 444 Giordano, D., Nichols, A. R., and Dingwell, D. B. (2005). Glass transition  
445 temperatures of natural hydrous melts: a relationship with shear viscosity  
446 and implications for the welding process. *JOURNAL OF VOLCANOLOGY  
447 AND GEOTHERMAL RESEARCH*, (1-2):105.
- 448 Global Volcanism Program (2017). Report on Momotombo (Nicaragua). In Ven-  
449 zke, E., editor, *Bulletin of the Global Volcanism Network*, volume 42:1, Smith-  
450 sonian Institution. <https://doi.org/10.5479/si.GVP.BGVN201701-344090>.
- 451 Gottsmann, J. and Dingwell, D. B. (2002). The thermal history of a spatter-fed  
452 lava flow: the 8-ka pantellerite flow of mayor island, new zealand. *Bulletin of  
453 Volcanology*, 64(6):410–422.
- 454 Greeley, R., Fagents, S. A., Scott Harris, R., Kadel, S. D., Williams, D. A.,  
455 and Guest, J. E. (1998). Erosion by flowing lava: Field evidence. *Journal of  
456 Geophysical Research*, (B11):27.
- 457 Head, J. W. and Wilson, L. (2017). Generation, ascent and eruption of magma  
458 on the Moon: New insights into source depths, magma supply, intrusions  
459 and effusive/explosive eruptions (Part 2: Predicted emplacement processes  
460 and observations). *Icarus*, 283(Lunar Reconnaissance Orbiter - Part II):176  
461 – 223.
- 462 Hill, B. E., Connor, C. B., Jarzempa, M. S., La Femina, P. C., Navarro, M., and  
463 Strauch, W. (1998). 1995 eruptions of cerro negro volcano, nicaragua, and  
464 risk assessment for future eruptions. *Geological Society of America Bulletin*,  
465 (10):1231.

- 466 Hobden, B. J., Houghton, B. F., and Nairn, I. A. (2002). Growth of a young,  
467 frequently active composite cone: Ngauruhoe volcano, New Zealand. *Bulletin*  
468 *of Volcanology*, (6):392.
- 469 Hurwitz, D. M., Fassett, C. I., Head, J. W., and Wilson, L. (2010). Formation  
470 of an eroded lava channel within an Elysium Planitia impact crater: Dis-  
471 tinguishing between a mechanical and thermal origin. *Icarus*, 210(2):626 –  
472 634.
- 473 Hurwitz, D. M., Head, J. W., and Hiesinger, H. (2013). Lunar sinuous rilles:  
474 Distribution, characteristics, and implications for their origin. *Planetary and*  
475 *Space Science*, 79-80:1–38.
- 476 Intercontinental Railway Commission (1898). A Condensed Report of the Trans-  
477 actions of the Commission and of the Surveys and Explorations of its Engi-  
478 neers in Central and South America.
- 479 Kauahikaua, J., Cashman, K. V., Mattox, T. N., Heliker, C. C., Hon, K. A.,  
480 Mangan, M. T., and Thornber, C. R. (1998). Observations on basaltic lava  
481 streams in tubes from Kilauea Volcano, island of Hawai'i. *Journal of Geophys-*  
482 *ical Research. Solid Earth*, 103(B11):27303.
- 483 Kerr, R. C. (2001). Thermal erosion by laminar lava flows. *Journal of Geophys-*  
484 *ical Research*, (11):26.
- 485 Kerr, R. C., Griffiths, R. W., and Cashman, K. V. (2006). Formation of chan-  
486 nelized lava flows on an unconfined slope. *Journal of Geophysical Research:*  
487 *Solid Earth (1978-2012)*, 111(B10).
- 488 Kilburn, C. R. J. and Lopes, R. M. C. (1988). The growth of AA lava flow  
489 fields on Mount Etna, Sicily. *Journal of Geophysical Research: Solid Earth*,  
490 93(B12):14759–14772.



- 491 Kirainov, V., Melekestev, I., Ovsyannikov, A., and Andreev, V. (1988). Re-  
492 construction of the eruptive activity of momotombo volcano (nicaragua) to  
493 assess volcanic hazards. pages 495 – 498.
- 494 Krieger, G., Moreira, A., Fiedler, H., Hajnsek, I., Werner, M., Younis, M.,  
495 and Zink, M. (2007). TanDEM-X: A Satellite Formation for High-Resolution  
496 SAR Interferometry. *IEEE Transactions on Geoscience and Remote Sensing*,  
497 (11):3317.
- 498 Miller, A. A. (1963). Free volume and viscosity of liquids: Effects of temperature.  
499 *The Journal of Physical Chemistry*, 67(5):1031–1035.
- 500 Patrick, M. R., Dehn, J., and Dean, K. (2004). Numerical modeling of lava  
501 flow cooling applied to the 1997 okmok eruption: Approach and analysis (doi  
502 10.1029/2003jb002537). *JOURNAL OF GEOPHYSICAL RESEARCH -ALL*  
503 *SERIES-*, (3):B03202.
- 504 Peterson, D. W., Holcomb, R. T., Tilling, R. I., and Christiansen, R. L. (1994).  
505 Development of lava tubes in the light of observations at Mauna Ulu, Kilauea  
506 Volcano, Hawaii. *Bulletin of Volcanology*, (5):343.
- 507 Richardson, P. and Karlstrom, L. (2019). The multi-scale influence of topogra-  
508 phy on lava flow morphology. *Bulletin of Volcanology*, (4):1.
- 509 Robl, J., Stwe, K., and Hergarten, S. (2008). Channel profiles around himalayan  
510 river anticlines: Constraints on their formation from digital elevation model  
511 analysis. *Tectonics*, 27(3).
- 512 Sapper, K. (1925). *Los volcanes de la America Central*. Halle: Verlag von Max  
513 Niemeyer.
- 514 Schenk, P. M. and Williams, D. A. (2004). A potential thermal erosion lava  
515 channel on Io. *Geophysical Research Letters*, 31(23).

- 516 Siewert, J. and Ferlito, C. (2008). Mechanical erosion by flowing lava. *Contem-*  
517 *porary Physics*, (1):43.
- 518 Sklar, L. and Dietrich, W. E. (1998). River Longitudinal Profiles and Bedrock  
519 Incision Models: Stream Power and the Influence of Sediment Supply. *Geo-*  
520 *physical Monograph - American Geophysical Union*, page 237.
- 521 Staude, S., Barnes, S. J., and Le Vaillant, M. (2017). Thermomechanical ero-  
522 sion of ore-hosting embayments beneath komatiite lava channels: Textural  
523 evidence from kambalda, western australia. *Ore Geology Reviews*, 90:446 –  
524 464.
- 525 Strozzi, T., Werner, C., Wiesmann, A., and Wegmuller, U. (2012). Topogra-  
526 phy Mapping With a Portable Real-Aperture Radar Interferometer. *IEEE*  
527 *Geoscience and Remote Sensing Letters*, (2):277.
- 528 Turcotte, D. L., Turcotte, D. L., and Schubert, G. (2002). *Geodynamics*. Cam-  
529 bridge ; New York : Cambridge University Press.
- 530 Vincent, F. (1890). In and out of Central America.
- 531 Voytenko, D., Dixon, T. H., Luther, M. E., Lembke, C., Howat, I. M., and de la  
532 Pea, S. (2015). Observations of inertial currents in a lagoon in southeastern  
533 Iceland using terrestrial radar interferometry and automated iceberg tracking.  
534 *Computers and Geosciences*, 82:23 – 30.
- 535 Williams, D. A., Kerr, R. C., and Lesher, C. M. (1998). Emplacement and  
536 erosion by archean komatiite lava flows at kambalda: Revisited. *Journal of*  
537 *Geophysical Research*, (B11):27.
- 538 Williams-Jones, G., Williams-Jones, A. E., and Stix, J. (1998). The nature  
539 and origin of Venusian canali. *Journal of Geophysical Research. Planets*,  
540 103(E4):8545.

- 541 Wilson, L. and Head, J. W. (2017). Generation, ascent and eruption of magma  
542 on the Moon: New insights into source depths, magma supply, intrusions and  
543 effusive/explosive eruptions (Part 1: Theory). *Icarus*, 283(Lunar Reconnaissance  
544 sance Orbiter - Part II):146 – 175.
- 545 Wooster, M. J., Wright, R., Blake, S., and Rothery, D. A. (1997). Cooling  
546 mechanisms and an approximate thermal budget for the 1991-1993 Mount  
547 Etna lava flow. *Geophysical Research Letters*, (24):3277.
- 548 Xie, S., Dixon, T. H., Voytenko, D., Fanghui, D., and Holland, D. M.  
549 (2018). Grounding line migration through the calving season at Jakobshavn  
550 Isbr, Greenland, observed with terrestrial radar interferometry. *Cryosphere*,  
551 12(4):1387 – 1400.

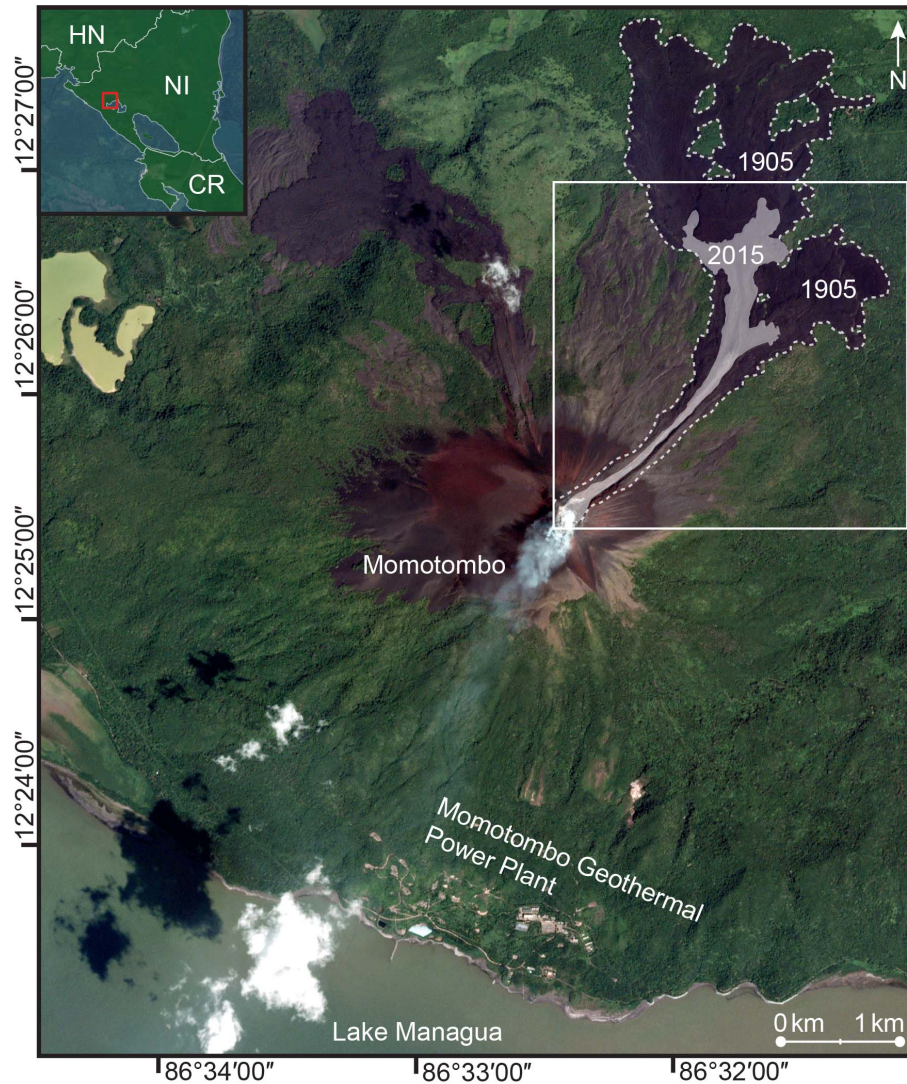


Figure 1: Momotombo area map. The most recent volcanism (a lava flow emitted during the 2015-2016 eruption) is noted by a light-grey overlay. The 1905 eruption is noted by a dotted line. The area shown in Fig. 4 is noted by the white box. Note the widely dispersed flows that underlie the 2015 and 1905 flows. Their distribution suggests that no incised channel existed at the time of their emplacement to direct flow paths. Background image from GoogleEarth.

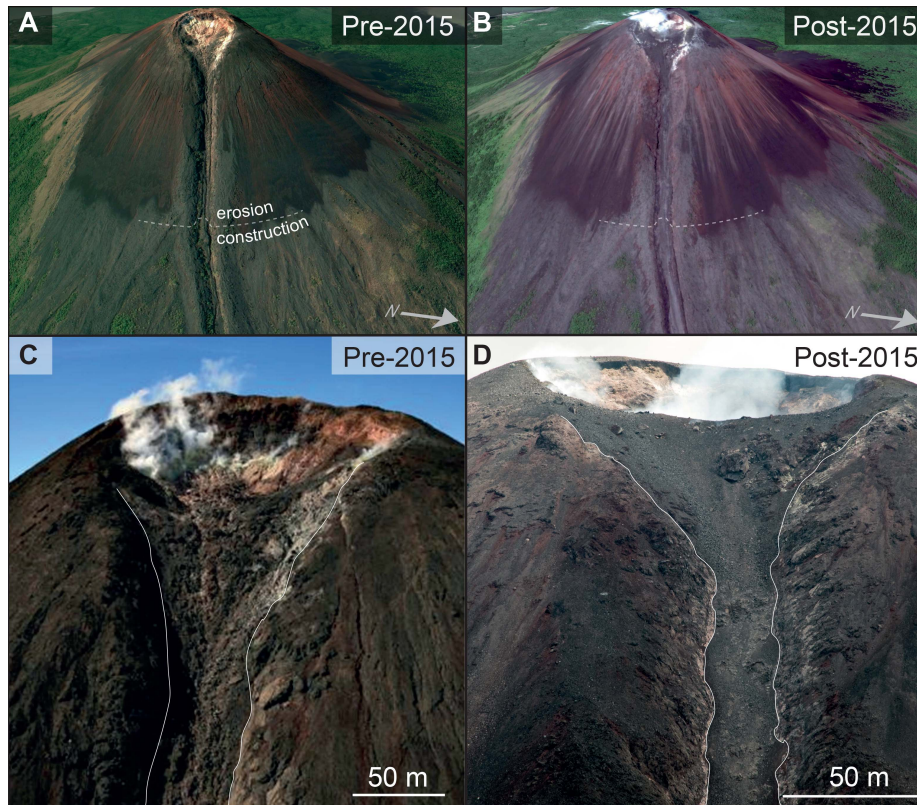


Figure 2: Pre and post 2015-2016 eruption images of the Momotombo channel and summit. A) A pre-eruption image of the channel, where the dashed line shows the approximate transition between erosional and constructional behavior. B) Major changes in morphology can be seen in and around the summit crater, where the 2015 lava flow first filled and was then partially excavated during subsequent explosions in 2016. The pre-existing floor of the channel has been paved over by a lava flow and appears less 'rough' than the pre-eruption channel floor. Images A and B from Google Earth. C) The summit crater prior to the 2015-2016 eruption, with white lines bounding the channel. Textures within the channel indicate downslope flow. Image from INETER. D) The summit area on 6 April, 2016. Several hundred small explosions have partially excavated a small dome from December, 2015. Blocks have been deposited atop the recent lava flow and a fine, grey layer of ash from repeated pyroclastic density currents coats the channel. Image from E. Gallant.

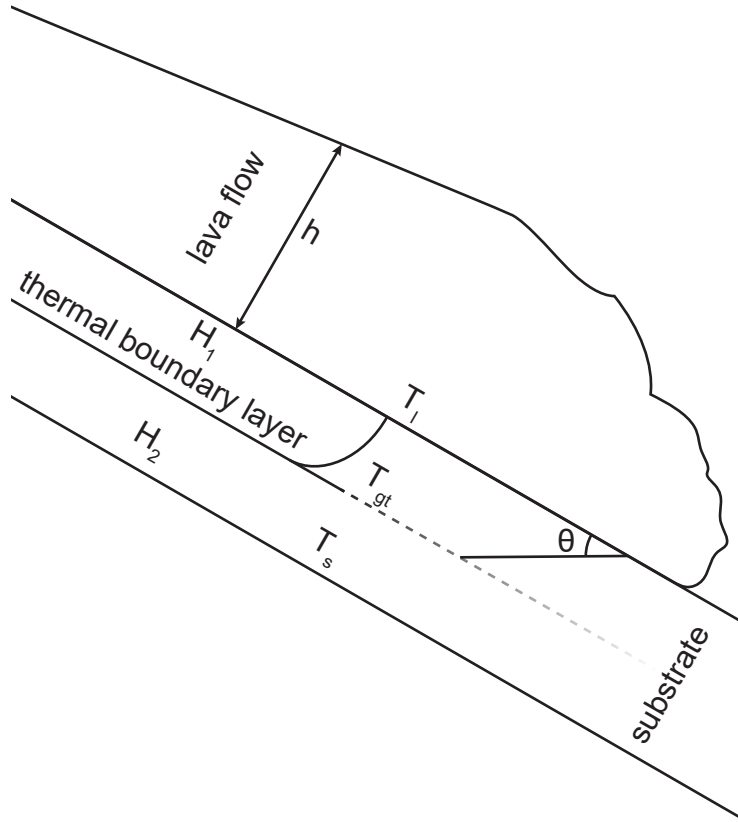


Figure 3: Thermal boundary formation illustration. The energy required to melt a pyroclast-rich substrate is less than that of a lava flow due to a lower density; we can therefore substitute the peak glass transition temperature (1013 K) as the minimum temperature required to initiate melting for such substrates (Giordano et al., 2005). The formation of the thermal boundary layer shows the transition between the temperature of the lava ( $T_l$ ) and the substrate ( $T_s$ ). This layer defines the boundary between a thermally softened substrate ( $H_1$ ) and the unaffected substrate ( $H_2$ ). The height of the lava flow is noted by  $h$  and the slope of the edifice by  $\theta$ .



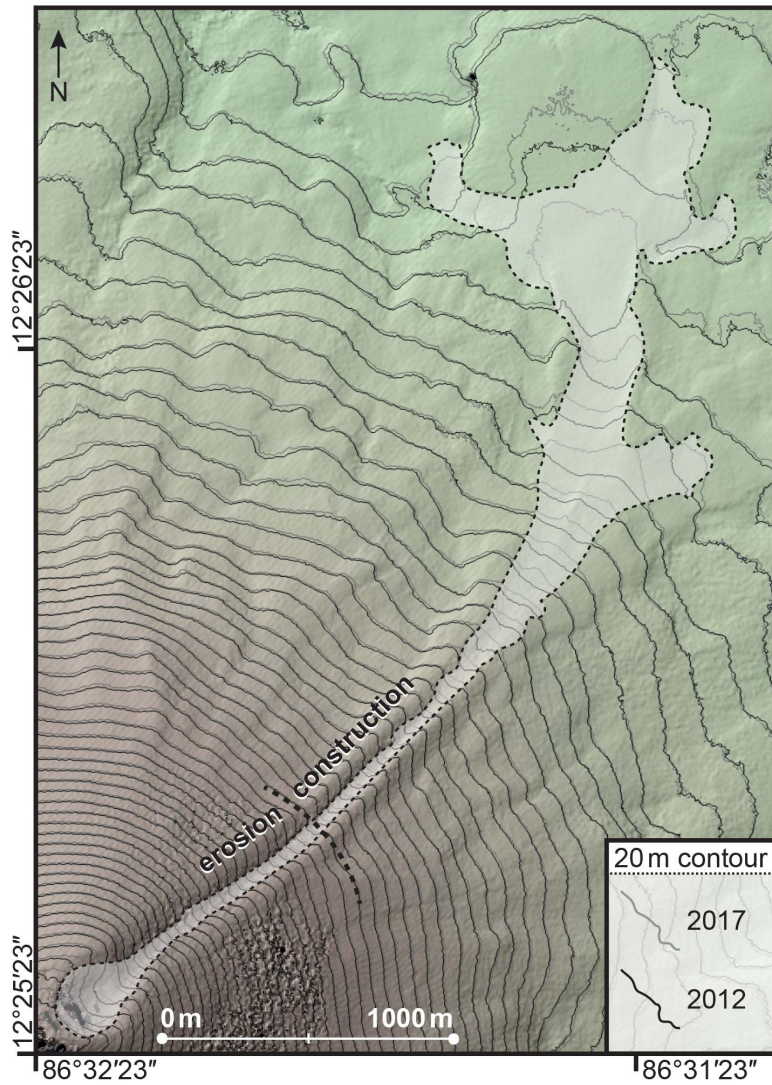


Figure 4: Elevation contour difference measured from the 2012 and 2017 TDX DEMs. Elevation contours at 20 m intervals were mapped from the TDX datasets; the grey contours represent the 2017 elevations (post 2015-2016 eruption), and the black represent the 2012 elevations. Slight contour variations exist in areas not impacted by the 2015-2016 eruption due to the different look angles of the TDX data pairs and georeferencing uncertainties. The dashed line and white infill show the area covered by the 2015 lava flow.

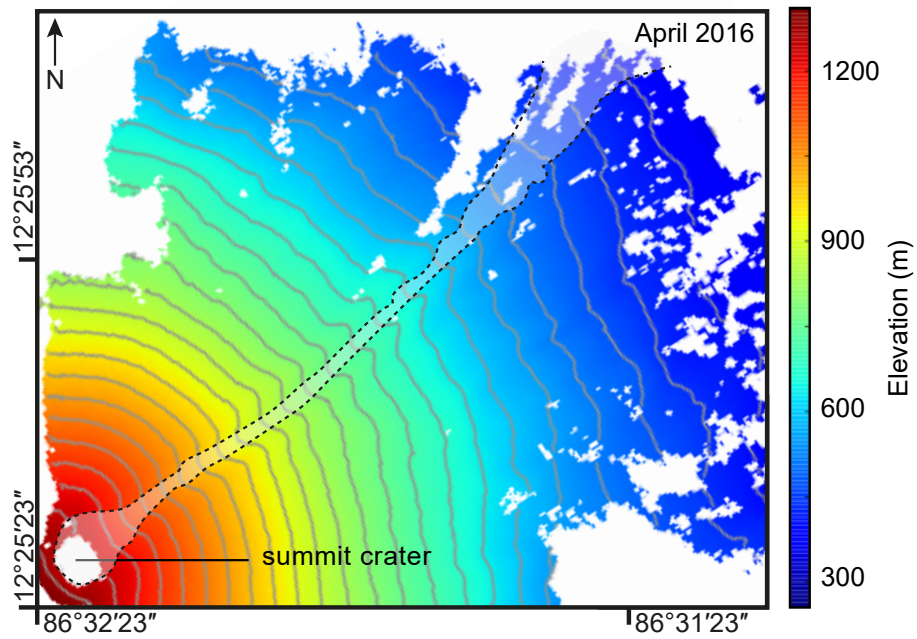


Figure 5: 2016 Terrestrial Radar DEM. The white infill and black dashed line shows the area covered by the 2015 lava flow. The absence of signal near the summit shows the  $120 \times 100$  m crater, which was excavated by several hundred small explosions between December 2015 and April 2016. The grey lines indicate 20 m contour intervals.



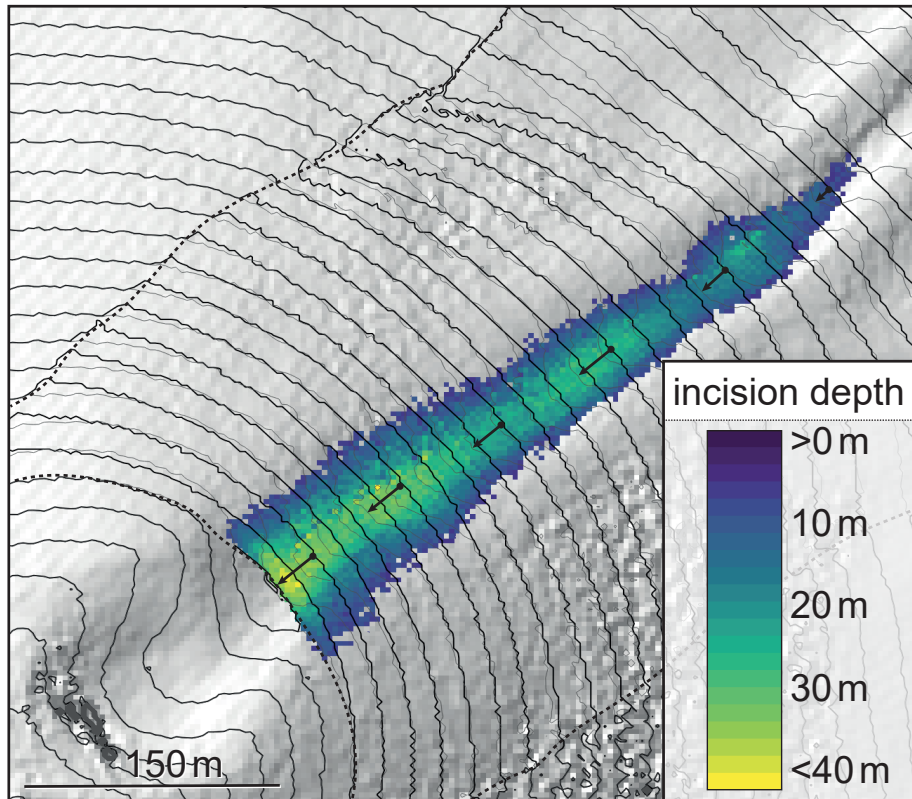


Figure 6: Elliptical contour fit incision depth process (from 2012 DEM). The original elevation contours at 20 m intervals are noted in grey, the modeled fit in black. Incision depths, with arrows that indicate the horizontal distance between the modeled paleotopography and the current point of corresponding incision. Incision is deepest at the summit and decreases downslope.

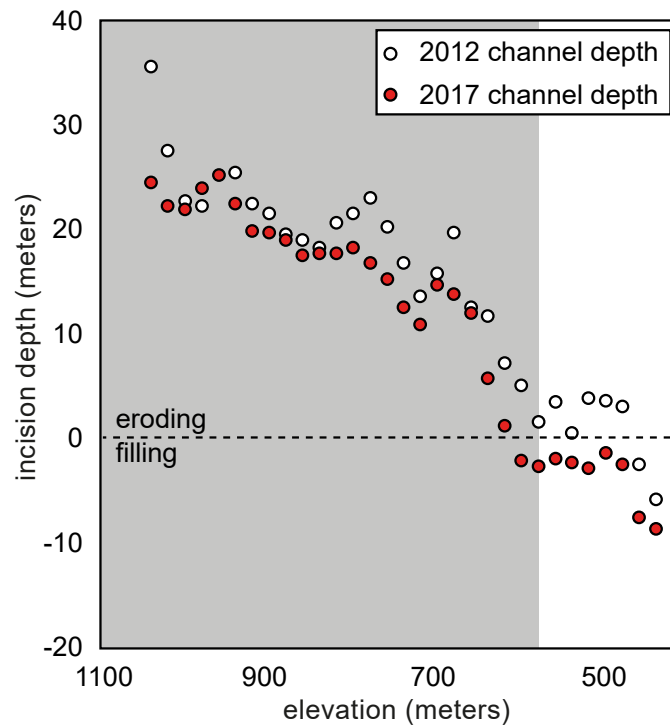


Figure 7: Calculated channel depths at 20-m elevation intervals before and after the eruption, using the elliptical fit method described in Figure 6. Calculated channel depths and slopes at 20-m elevation intervals before and after the eruption. White and red dots are channel depths of the pre- and post-eruption channel, respectively. The difference of the two DEMs gives us the thickness of the 2015 lava flow. The grey shading indicates the elevation range where erosion dominates ( $>650$  m).

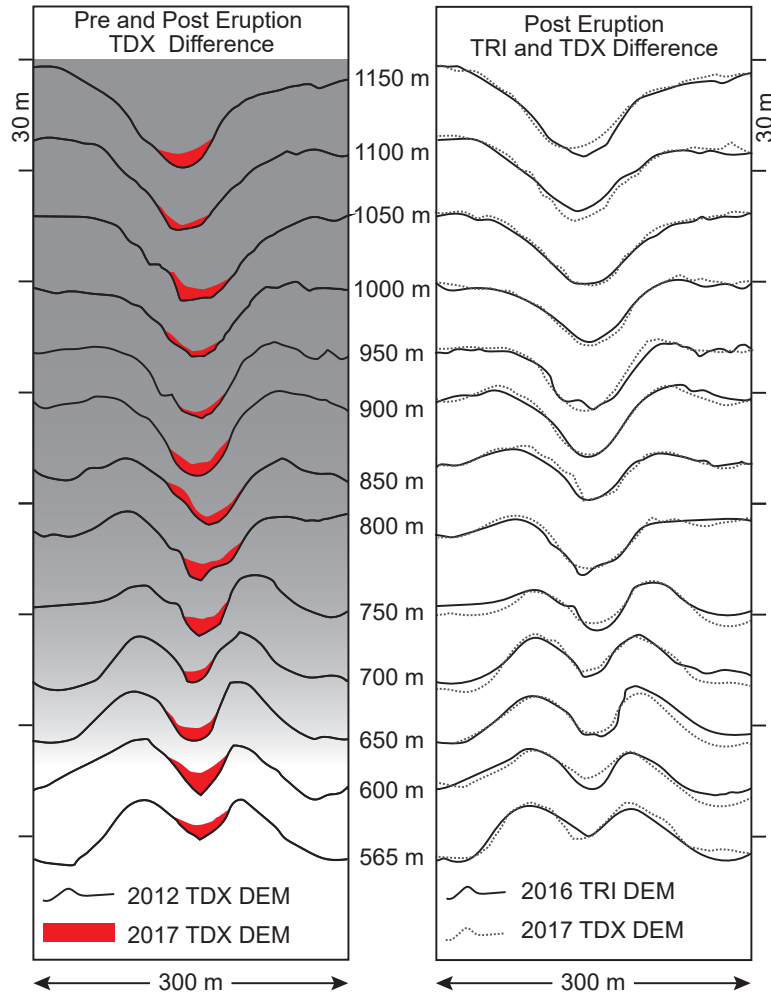


Figure 8: Momotombo lava channel profiles. The left figure shows channel profiles from the 2012 TDX DEM and an overlay of the lava flow from 2015. The 2012 profile is noted by the solid black line, with the 2015 lava flow (imaged by the 2017 TDX acquisition) by the red polygon. The grey shading illustrates the transition of channel into a constructional feature. The profiles have been visually adjusted to match up topography in order to account for the  $21^\circ$  difference in acquisition angles. The right figure shows the difference between the 2016 TRI DEM and the 2017 TDX DEM. Comparison of the post-eruption profiles estimates the relative noise of the DEMs.

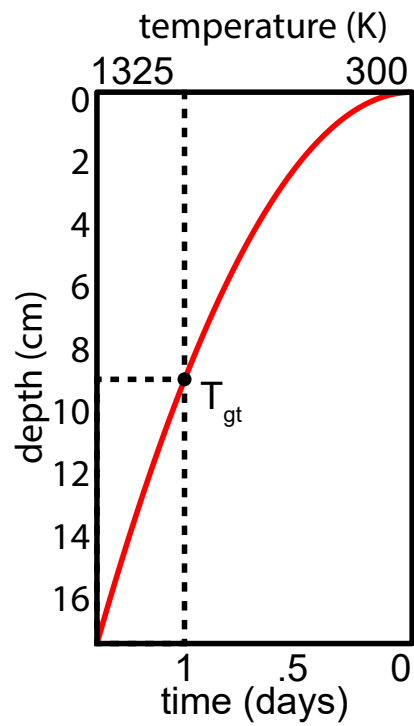


Figure 9: Substrate thermal boundary layer. At one day, we calculate the thermal boundary layer for a flow on Momotombo to grow to 8.8 cm. Thermal erosion rates in Hawaiian tubes and channels can reach  $\sim 10$  cm per day (Kauahikaua et al., 1998); given the lower temperature of lavas erupted on Momotombo, it is reasonable to assume a slower rate of thermal boundary growth.

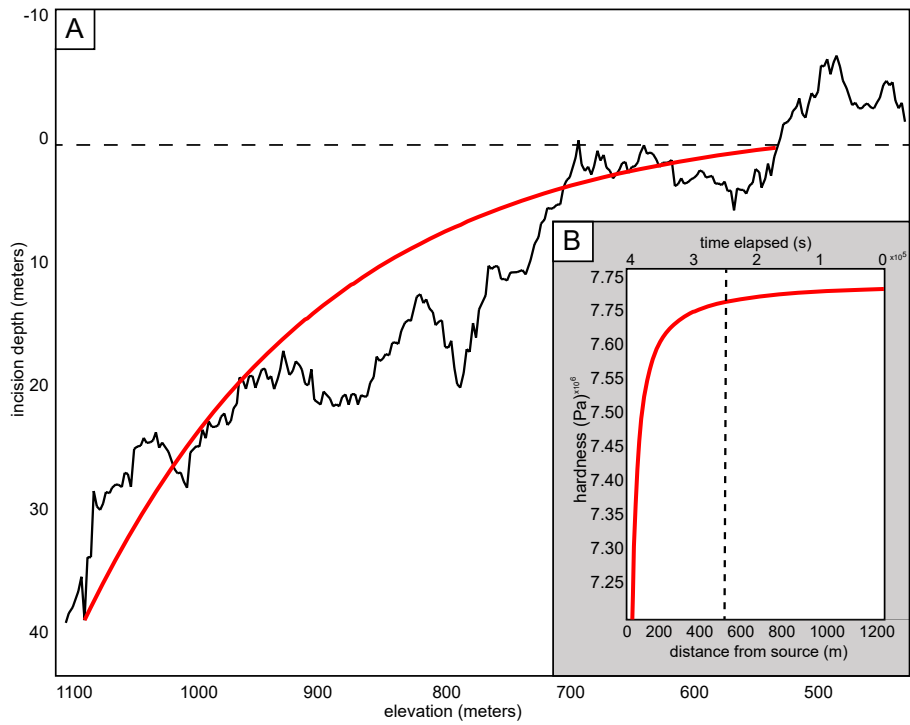


Figure 10: Incision depth fit models. A: Depth is used as a proxy for time in order to constrain the hardness ( $H$ ) of the eroded substrate. The red line indicates the exponential fit to the eroded depth as a function of elevation. The dotted line indicates the the transition from erosion (below) to construction (above). B: Substrate hardness as a function of time and distance. The dotted line notes the transition from erosion (left) to construction (right). Time elapsed is the total time the substrate is in contact with flowing lava.

552 **Supplemental Material**

553 **Paleotopography Modeling Code**

554 The MatLab code and associated functions used to model the paleotopogra-  
555 phy of the erosive channel and determine excavation depths is available at  
556 [https://github.com/elisabeth-gallant/USF\\_dissertation](https://github.com/elisabeth-gallant/USF_dissertation).

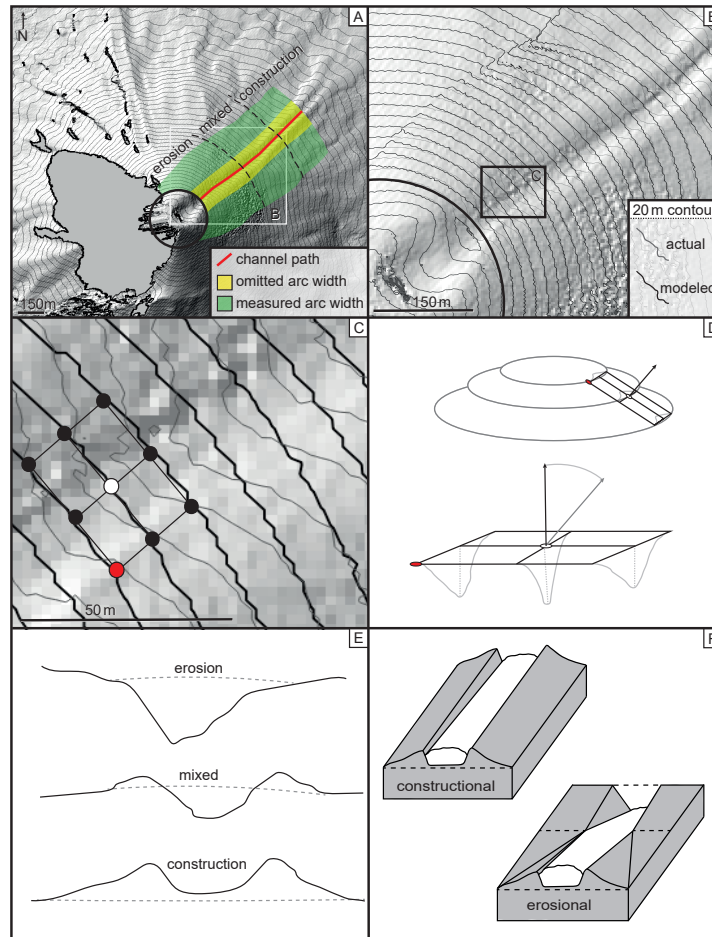


Figure 11: Elliptical contour fit incision depth process (from 2012 DEM). A: The center of the channel is noted in red, area used to calculate the best fit contours in green, and the area omitted from the contour calculation in yellow. The dashed line shows the approximate boundary between erosional, mixed, and constructional regimes (described in profile in panel F). B: The original elevation contours at 20 m intervals are noted in grey, the modeled fit in black. C: The orientation of vectors normal to the edifice are calculated using a  $9 \times 9$  matrix. The distance between sampling points is enlarged to illustrate the concept. D: The matrix is transposed so that the only magnitude of the vector is in the z-direction. The elevation value is returned as a weighted-average of the constituent points (with distance from the center as the weighting criteria). E: The simplified profiles for erosional, mixed, and constructional regimes, with a dashed line denoting the paleosurface. F: Constructional (left) vs erosional (right) behaviour in lava channels on an incline. We note the change in slope associated with the original orientation of the incline and the eroded portion. The dashed line notes the paleotopography surface. Additionally, levees are absent from the incised section of the channel. Profiles of these different regimes are presented in Figure 8.

557 **Circular Contour Fit**

558 Channel incision depths were measured by interpolating best-fit 20-m interval  
559 contour lines to the overall shape of the edifice using the 2012 TDX DEM. Each  
560 interpolated contour line was calculated by fitting the original contour line with  
561 an arc using least-squares. The section proximal to the channel was not included  
562 in the fitting process due to its wide deviation from the overall shape of the cone.  
563 Depth at each sampled elevation was measured by determining the minimum  
564 distance between the interpolated contour line and the deepest point of the  
565 channel, measured normal to the slope of the edifice (Fig. 12b). All points on  
566 the contour line (not including the flow levees and the channel) were averaged  
567 to calculate the slope for each measured depth.

568 Results show the pre-2015 eruption channel extended down the northeast  
569 side of the edifice from the summit and continued for 2 km onto the surrounding  
570 plain (Fig. 13). A consistent width of  $\sim 30$  m was maintained throughout the  
571 channels length, while incision depth varied from 35 m at the summits rim and  
572 tapered off to 0 at  $\sim 700$  m elevation (Fig. 12a). The 1905 channel has been  
573 infilled with a lava flow from 2015 with a thickness  $< 3$  m (Fig. 13).



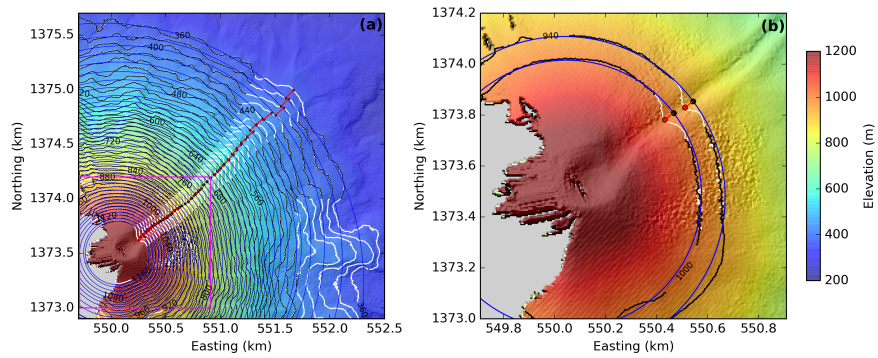


Figure 12: Channel depth calculation using the pre-eruption DEM as an example (a) 2012 DEM. Black and white lines are contours with 20 m interval. The blue circles are the best-fit arcs for each contour line. Contour lines in white were not used in the fitting processing because they include the topographic influence of the levees and channel, which greatly deviates from the circular fit. The red lines indicate the depth of the channel thalweg. (b) A zoomed in view of the fitting process. Red dots indicate the deepest points in the channel.

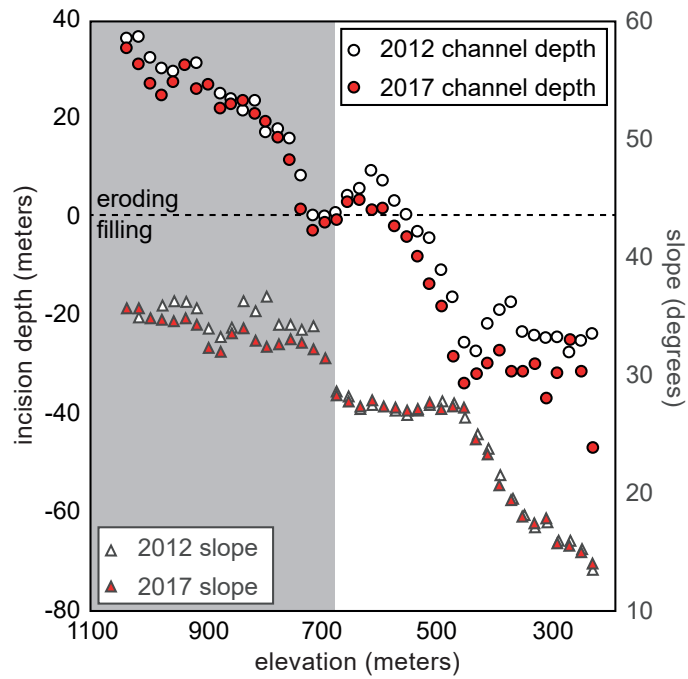


Figure 13: Calculated channel depths, slopes, and differences using the circular fit method. Calculated channel depths and slopes at 20-m elevation intervals before and after the eruption. White and red dots are channel depths of the pre- and post-eruption channel, respectively. The difference of the two DEMs gives us the thickness of the 2015 lava flow. White and red triangles are averaged slopes at 20-m elevation intervals of the pre- and post-eruption edifice.

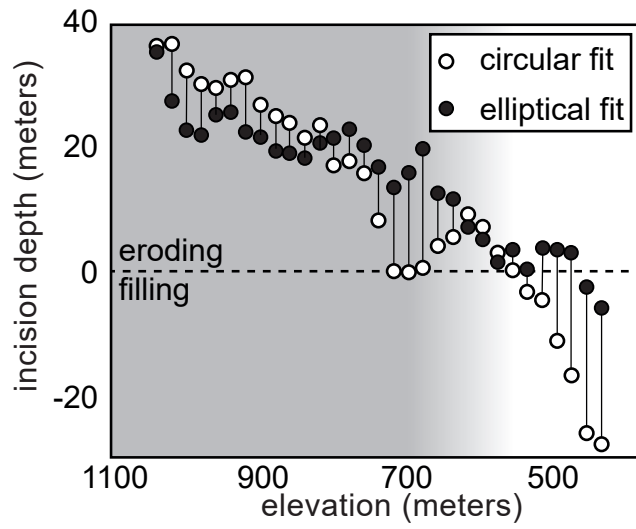


Figure 14: Comparison of the circular and elliptical method incision depths for the 2012 TDX DEM. The grey area indicates the transition between incision and construction, with a gradient to indicate the uncertainty between the two models as to where this occurs.